TUNING OF GRAPHITIC CARBON NITRIDE FOR ENHANCEMENT IN PHOTOCATALYTIC DEGRADATION OF TETRACYCLINE HYDROCHLORIDE

Dissertation submitted to
Visvesvaraya National Institute of Technology, Nagpur
in partial fulfilment of the requirements for the award of the degree

Master of Science
in
Chemistry

by

SAUMYA MEGHWANI
(MS23CHM013)

Under the guidance of
Dr. Atul V. Wankhade

Department of Chemistry
Visvesvaraya National Institute of Technology
Nagpur 440010 (India)

May 2025

©Visvesvaraya National Institute of Technology (VNIT) 2025

Department of Chemistry
Visvesvaraya National Institute of Technology, Nagpur

Declaration

I, **Saumya Meghwani**, hereby declare that this dissertation titled "**Tuning of Graphitic Carbon Nitride for Enhancement in Photocatalytic Degradation of Tetracycline Hydrochloride**" is carried out by me in the Department of Chemistry of Visvesvaraya National Institute of Technology, Nagpur. The work is original and has not been submitted earlier, whole or in part, for the award of any degree/diploma at this or any other institute or university.

Saumya Meghwani
Date:

Department of Chemistry
Visvesvaraya National Institute of Technology, Nagpur

Certificate

This is to certify that the dissertation titled "**Tuning of Graphitic Carbon Nitride for Enhancement in Photocatalytic Degradation of Tetracycline Hydrochloride**" is submitted by **Saumya Meghwani** in partial fulfilment of the requirements for the award of the degree of **Master of Science in Chemistry**, VNIT Nagpur. The work is comprehensive, complete, and fit for final evaluation.

Dr. Atul V. Wankhade
Associate Professor,
Department of Chemistry,
VNIT, Nagpur.

Prof. Sujit K. Ghosh
Head of Department,
Department of Chemistry,
VNIT, Nagpur.
Date:

Visvesvaraya National Institute of Technology, Nagpur

Department of Chemistry

Non-Plagiarism Certificate

Certified that M.Sc. dissertation titled "**Tuning of Graphitic Carbon Nitride for Enhancement in Photocatalytic Degradation of Tetracycline Hydrochloride**" submitted by **Saumya Meghwani** has been checked for plagiarism using TURNITIN software and overlap is found within prescribed limits. A summary of the report is given below.

ORIGINALITY REPORT

14%	9%	12%	%
SIMILARITY INDEX	INTERNET SOURCES	PUBLICATIONS	STUDENT PAPERS

Saumya Meghwani
(MS23CHM013)

Dr. Atul V. Wankhade
Associate Professor,
Department of Chemistry,
VNIT, Nagpur
(440010)

ACKNOWLEDGEMENT

I, **Saumya Meghwani** would like to express my sincere gratitude to my supervisor **Dr. Atul V. Wankhade** for his invaluable guidance and support throughout my journey as a M.Sc. student. His astute insights, constructive feedback and visionary guidance have been instrumental in shaping the direction of my work. He had consistently challenged me to think critically, encouraged me to explore new avenues of inquiry, and inspired me to reach for excellence.

I would like to acknowledge Department of Chemistry, VNIT, Nagpur, teaching and non-teaching staff for their support and assistance during my project.

I would like to extend my special thanks to **Ms. Awanti Talmale**, whose significant contributions and expert guidance greatly impacted the success of my project. Her support and assistance were invaluable, and I am grateful for the time and effort she invested in helping me achieve my research goals.

I am thankful to my seniors Mr. Adarsh Mourya, Mr. Mohd Amin, Ms. Sakshi Barad, Ms. Diksha Mohod, Mr. Manoranjan and my lab-mate Mr. Himanshu for their help, encouragement, and camaraderie. They created a lively and supportive environment in the lab, making my research experience enjoyable and productive.

Finally, I would like to express my deepest gratitude to my family and friends for their unwavering support and encouragement throughout my academic journey. Their presence and love were a constant source of motivation and inspiration.

Saumya Meghwani

ABSTRACT:

Environmental contamination caused by antibiotics, such as Tetracycline Hydrochloride (TCH), has become a growing concern amidst affecting aquatic ecosystems and posing risks to human and animal health. This challenge is compounded by the broader issues of climate change and the urgent need for sustainable environmental solutions. Among the innovative approaches being explored, solar-driven photocatalysis has emerged as a promising and eco-friendly method for tackling such pollutants. In this study, we report the synthesis of novel heterostructure comprising Zinc Indium Sulfide ($ZnIn_2S_4$) loaded on Fluorinated graphitic Carbon Nitride (F-g-C_3N_4) using a solvothermal method. Advanced characterization techniques including X-ray diffraction (XRD), UV-Vis diffuse reflectance spectroscopy (UV-DRS), Brunauer–Emmett–Teller (BET) surface area analysis, Thermogravimetric Analysis (TGA), X-ray photoelectron spectroscopy (XPS), Field Emission Scanning Electron Microscopy (FE-SEM), and Transmission Electron Microscopy (TEM) were employed to analyse the structure, morphology, and properties of the synthesized heterostructure $ZnIn_2S_4$/F-g-C_3N_4. The 30% $ZnIn_2S_4$/F-g-C_3N_4 nanocomposite demonstrated exceptional photocatalytic activity in comparison to nanocomposite 10%, 20%, and 40% nanocomposites achieving 90% degradation of TCH within 90 minutes (rate constant, $k = 0.026\ min^{-1}$) under visible light irradiation. The degradation mechanism was further investigated through quenching study, which reveals that the superoxide radicals are the prominent reactive species driving the degradation of TCH. These results highlight the material's effectiveness in addressing water contamination caused by antibiotics and contribute to advancing sustainable solutions for environmental protection.

List of Figures:

Fig. no.	Figures	Page no.
	Chapter 1	
1.	Comparison of Nanomaterials on length scale.	1
2.	Categorization of nanomaterials according to their dimensional properties.	2
3.	Synthesis approach of Nanomaterials	5
4.	Waste water from various sectors.	6
	Chapter 2	
5.	Synthesis and Structure of g-C_3N_4 (g-CN).	11
6.	Synthesis of F-g-C_3N_4 (F-gCN).	12
7.	Synthesis of $ZnIn_2S_4$ (ZIS).	13
8.	Synthesis of $ZnIn_2S_4$/F-g-C_3N_4 (ZIS/F-gCN).	14
	Chapter 3	
9.	PXRD pattern of gCN, F-gCN, ZIS, and ZIS/F-gCN composites.	16
10.	FESEM images of gCN **(a-b)**, F-gCN **(c-d)**, ZIS/F-gCN **(e-f)**	17
11.	**(g)** EDS analysis and **(h)** Elemental mapping.	18
12.	UV-Vis DRS Spectrum.	19
13.	Kubelka-Munk plots of gCN, F-gCN, ZIS/F-gCN with varying ZIS loadings.	19

14.	Full scan and high-resolution XPS survey spectra of 30% ZIS/F-gCN.	20
15.	Full scan and high-resolution XPS spectra of (i) Zn 2p (ii) In 3d (iii) S 2p (iv) F 1s (v) C 1s (vi) N 1s.	20
16.	HR-TEM images of 30% ZIS/F-gCN.	21
17.	Thermogravimetric Analysis of 30% ZIS/F-gCN.	22
18.	N_2 adsorption-desorption isotherm for 30% ZIS/F-gCN.	23
19.	Pore size distribution of 30% ZIS/F-gCN.	23
	Chapter 4	
20.	**(a)** TCH Degradation experiments for blank (no catalyst), gCN, F-gCN, ZIS/F-gCN composites with varying ZIS loadings. **(b)** Rate constant plot for gCN, F-gCN, ZIS/F-gCN composites with varying ZIS loadings.	25
21	**(a)** Effect of catalyst dose on photocatalytic TCH degradation using 30% ZIS/F-gCN composite under visible light irradiation (20 mg L^{-1}, 100 mL, pH 6) **(b)** Effect of initial pH on photocatalytic TCH degradation using 30% ZIS/F-gCN composite under visible light irradiation (20 mg L^{-1}, 100 mL, 50 mg catalyst) TCH degradation Optimization for (a) catalyst dose and (b) pH conditions.	25
22.	Plausible Mechanism for TCH degradation.	27
23.	Quenching Experiment for TCH degradation.	27
24.	The recyclability test of photocatalytic TCH degradation for 30% ZIS/F-gCN.	28

Contents:

S. no.	Contents	Page no.
	Chapter 1 **Introduction to Nanomaterials and Literature Survey**	
1.1.	What are Nanomaterials?	1
1.2.	Classification of Nanomaterials	2
1.3.	Synthesis of Nanomaterials	4
1.4.	Water Pollution	6
1.5.	Sources of Water Pollution	7
1.6.	Several techniques used for the decontamination of water	7
1.7.	Literature Review	9
	Chapter 2 **Experimental Section**	
2.1.	Chemicals used	11
2.2.	Synthesis:	11
2.2.1.	Synthesis of graphitic carbon nitride (g-C_3N_4)	11
2.2.2.	Synthesis of fluorinated-graphitic carbon nitride (F-g-C_3N_4)	11
2.2.3.	Synthesis of Zinc Indium Sulfide ($ZnIn_2S_4$)	12
2.2.4.	Synthesis of $ZnIn_2S_4$/F-g-C_3N_4 (ZIS/F-gCN) Composites	13
2.3.	Characterization	14
2.4.	Photocatalytic Activity Evaluation	15

	Chapter 3 **Results and Discussion**	
3.1.	Powder X-Ray Diffraction (PXRD)	16
3.2.	Field Emission Scanning Electron Microscopy (FE-SEM)	17
3.3.	UV-Vis Diffuse Reflectance Spectroscopy (UV-DRS)	18
3.4.	X-Ray Photoelectron Spectroscopy (XPS)	20
3.5.	High-Resolution Transmission Microscopy (HR-TEM)	22
3.6.	Thermogravimetric Analysis (TGA)	22
3.7.	Brunauer-Emmett-Teller Analysis (BET)	23
	Chapter 4 **Photocatalytic Experiments**	
4.1.	Photocatalytic degradation of TCH	25
4.2.	Plausible Mechanism	27
4.3.	Recyclability Test of the Photocatalyst	29
	Conclusion	30
	References	31
	Future Scope	36

CHAPTER I

Introduction to Nanomaterials and Literature Survey

Introduction

Nanoscience and nanotechnology are built upon the foundation of nanomaterials, which have unique properties that differ significantly from their bulk counterparts. The rapid growth of research and development in this interdisciplinary field has led to significant advancements in synthesis, characterization, and fabrication techniques. Nanomaterials have potential applications across multiple domains, such as electronics, healthcare, energy, and materials science. Notably, they also hold promise for environmental remediation, particularly bioremediation, where nanoparticles can be designed to target and degrade pollutants, offering innovative solutions for cleaning contaminated sites. The commercial impact of nanoscience and nanotechnology is substantial, with applications in consumer products, healthcare, energy, and industrial processes. As research continues to advance, the field is expected to drive innovation and economic growth, with its impact undoubtedly growing in the future. Advancing novel nanomaterials, refining synthesis approaches, and enhancing characterization techniques will be instrumental in shaping the future of nanoscience and nanotechnology.

1.1. What are Nanomaterials?

Nanomaterials are substances with dimensions ranging between 1 and 100 nanometers in at least one direction. These materials exhibit unique optical, magnetic, electrical, and other characteristics that show a marked contrast to those of conventional bulk materials, making them highly valuable. Examples encompass metals, ceramics, polymers, as well as carbon-based substances such as graphene and carbon nanotubes.

Nanomaterials can be produced using methods such as chemical synthesis, physical vapor deposition, or self-assembly. Because of their minuscule dimensions and distinctive properties, they find extensive applications in various fields like electronics, medicine, energy, and environmental remediation. Their versatility and enhanced performance over traditional materials have driven major advancements in science and technology.

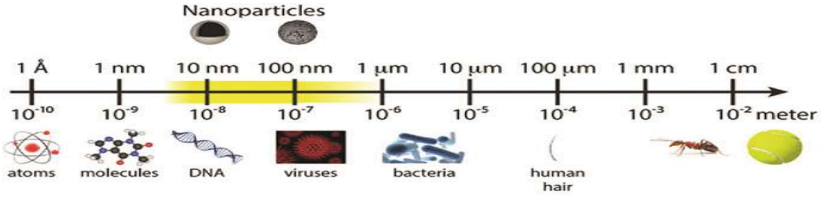

Fig. 1 Comparison of Nanomaterials on length scale.

1.2. Classification of Nanomaterials

Nanomaterials can be classified based on their structure, composition, and dimensionality. Here are some common classifications of nanomaterials.

1.2.a. Dimensionality:

Nanomaterials are classified based on the number of dimensions that fall within the nanoscale range, determining their distinct properties and applications.

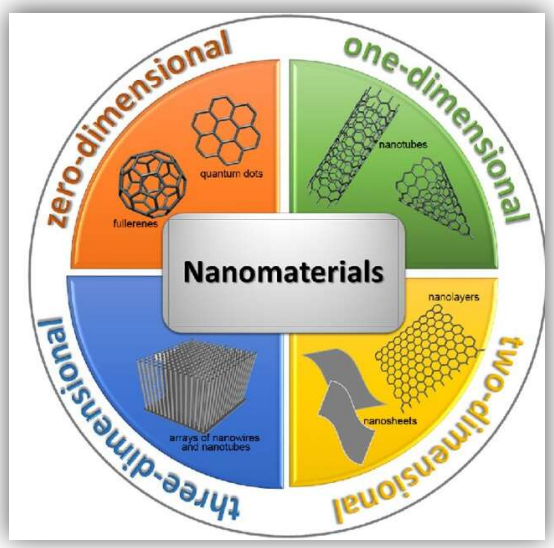

Fig. 2 Categorization of nanomaterials according to their dimensional properties.

- **Zero-dimensional (0D) nanomaterials:** These materials typically have dimensions between 1 to 10 nanometers, with all three dimensions confined to the nanoscale. Examples include nanoclusters, which consist of small groups of atoms, fullerenes, which are spherical carbon molecules, and quantum dots, which are semiconductor nanoparticles known for their unique optical characteristics.
- **One-dimensional (1D) nanomaterials:** These materials possess a single dimension beyond the nanoscale range, while the remaining two stay within it. Examples include nanowires, which are cylindrical in shape, nanotubes, which are hollow cylindrical structures, and nanorods, which are needle-like in form. These materials are often characterized by exceptional mechanical and electrical properties.

- **Two-dimensional (2D) nanomaterials:** These materials have one dimension within the nanoscale range, while the other two dimensions exceed it. Examples comprise graphene, consisting of carbon atoms systematically positioned in a hexagonal framework, transition metal dichalcogenides, which are layered materials with distinct electronic properties, and nanosheets. They are recognized for their extensive surface area and unique optical and electrical characteristics.
- **Three-dimensional (3D) nanomaterials:** Nanomaterials that are not restricted to the nanoscale in any dimension have all three dimensions exceeding 100 nanometers. Examples comprise spherical nanoparticles, nanocrystals (crystals with nanoscale dimensions), dendrimers, and liposomes.

1.2.b. Morphology:

Nanomaterials can also be categorized based on their shape or morphology:

- **Spherical:** Used in imaging and catalysis, examples include nanoparticles and fullerenes.
- **Tubular:** Applied in drug delivery and electronics, such as nanotubes and nanorods.
- **Fibrous:** Essential for filtration and composites, like nanowires and nanofibers.
- **Plate-like:** Utilized in energy storage and optoelectronics, examples are graphene and nanosheets.
- **Dendritic:** Found in drug release and catalysis, such as dendrimers.

1.2.c. Composition

Nanomaterials are categorized by their chemical composition, which determines their unique properties and uses:

- **Metal Nanomaterials:** Comprising nanoparticles, nanowires, and nanotubes made from metals like gold, silver, and platinum, these excel in catalysis, electrical conductivity, and optical performance.
- **Semiconductor Nanomaterials**: Including quantum dots, nanowires, and nanoparticles of materials like silicon and gallium nitride, they are integral to electronic and optoelectronic applications.

- **Ceramic Nanomaterials:** Consisting of oxides and nitrides in the form of nanoparticles or nanocrystals, these are valued for their durability, thermal stability, and resistance to wear.
- **Carbon-Based Nanomaterials:** Featuring graphene, carbon nanotubes, and fullerenes, these stand out for their conductivity, mechanical strength, and thermal efficiency.
- **Polymer-Based Nanomaterials:** Made from polymer-based nanoparticles and nanofibers, they are widely used in drug delivery, biocompatible applications, and protective coatings.

1.3. Synthesis of Nanomaterials

The synthesis of nanomaterials involves techniques designed to control their size, shape, and properties. These approaches are broadly classified into two main categories: top-down and bottom-up methods.[1]

- **Top-down approach**

  The top-down approach involves reducing bulk materials to nanoscale structures using techniques like mechanical milling, lithography, and etching. It is effective for large-scale production and precise shape control, making it useful in industries like electronics. However, it may cause surface defects, limited atomic precision, and material waste. Despite these challenges, it remains essential for structured nanomaterial synthesis.

- **Bottom-up approach**

  The bottom-up approach to nanomaterial synthesis involves assembling nanostructures atom by atom or molecule by molecule, enabling meticulous regulation of their dimensions, structure, and characteristics. Mimicking natural processes, this method enables the creation of high-purity materials with minimal defects. Techniques such as chemical vapor deposition (CVD), sol-gel processes, hydrothermal synthesis, and self-assembly are commonly employed in this approach. CVD involves depositing thin films through gas-phase reactions, while sol-gel processes create nanostructures through chemical solution gelation.

Hydrothermal synthesis uses controlled temperature and pressure to grow nanocrystals, and self-assembly relies on molecular interactions to form nanoscale structures. The bottom-up approach is particularly suited for applications requiring atomic-level precision, such as in electronics, energy devices, and advanced materials. While this method often requires specialized conditions and slower processes, its ability to produce tailored nanomaterials with exceptional properties makes it integral to nanotechnology.

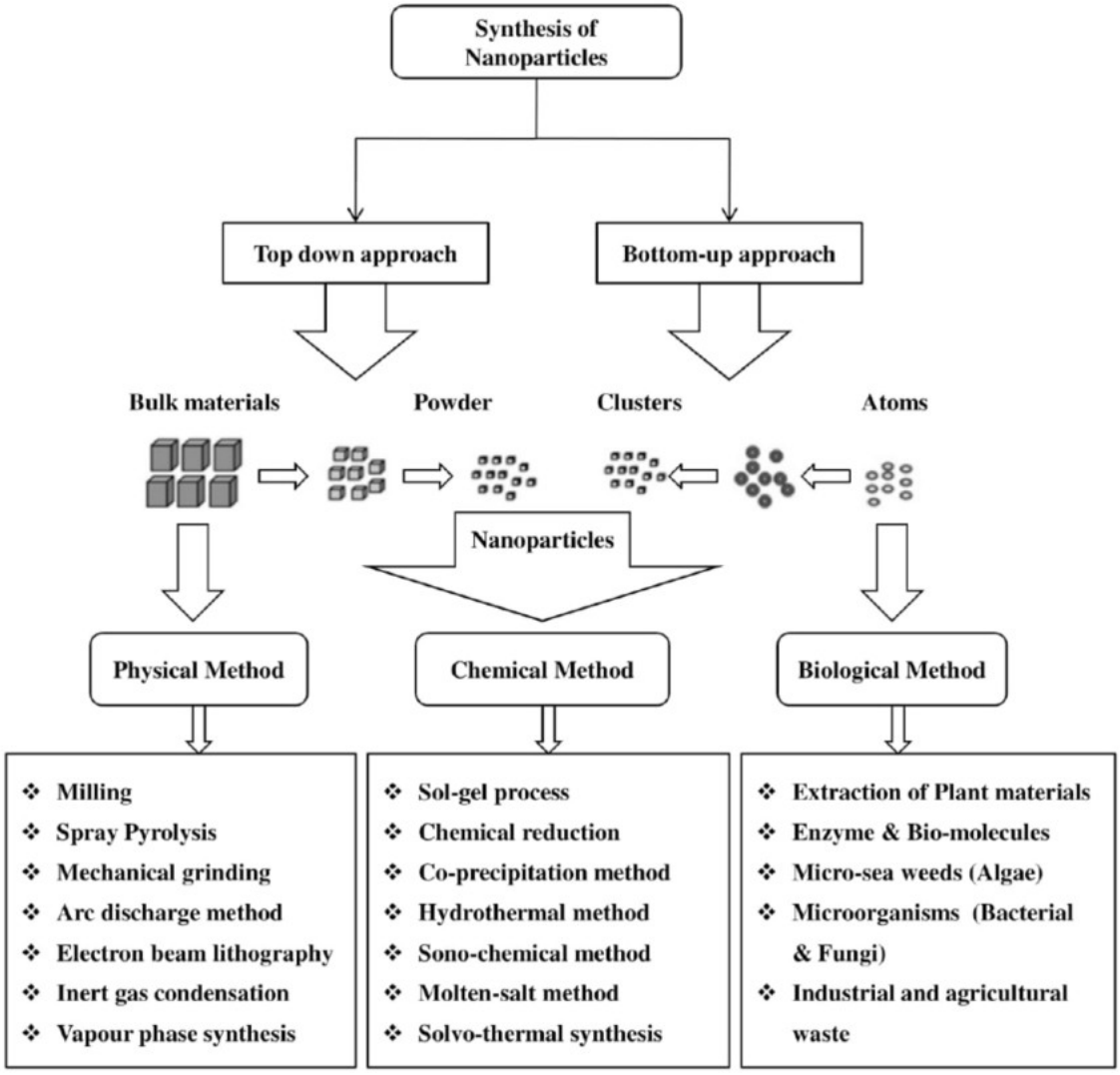

Fig. 3 Synthesis approach of Nanomaterials.

1.4. Water Pollution

Water pollution is a pressing global issue, necessitating continuous reassessment of water resource management policies to mitigate its impact. Widespread contamination of water bodies leads to numerous health risks and fatalities, with an estimated 14,000 deaths occurring daily due to waterborne diseases. Pollution originates from diverse sources such as industrial effluents, agricultural runoff, untreated wastewater, and household waste. Among emerging contaminants, antibiotics pose a significant threat due to their persistence in the environment and their role in fostering antimicrobial resistance. [2] [3] Tetracycline Hydrochloride (TCH), widely used in veterinary and human medicine, has been frequently detected in water bodies, contributing to ecological imbalances and potential health hazards. Exposure to residual antibiotics in contaminated water can disrupt microbial communities, impact aquatic life, and lead to bioaccumulation in the food chain. Additionally, prolonged human exposure to antibiotic-laden water has been linked to adverse health effects, including resistance development and organ toxicity. In conclusion, antibiotic pollution, particularly from substances like TCH, presents a serious environmental challenge, threatening ecosystems and public health. Understanding its sources and implications is critical for designing effective remediation strategies and safeguarding water resource.

(a) (b)

Fig. 4 (a & b) Waste water from various sectors.

1.5. Sources of Water Pollution

Water pollution arises from numerous sources, both anthropogenic and natural. Industrial facilities, agricultural activities, sewage discharge, and urban runoff are primary contributors. Effluents from industries often contain hazardous chemicals, heavy metals, and organic pollutants, which are inadequately treated before entering water bodies. Similarly, untreated sewage from urban and rural areas introduces harmful microorganisms, chemicals, and waste into rivers and lakes. Agricultural practices, including excessive use of pesticides, fertilizers, and improper disposal of animal waste, further add to the contamination. Urban runoff from impermeable surfaces like roads and rooftops carries pollutants such as oils, chemicals, and debris into aquatic ecosystems. These pollutants collectively degrade water quality, endanger aquatic organisms, and present significant health hazards to humans.[4] [5]

The pollution of water bodies with antibiotics such as Tetracycline Hydrochloride (TCH) originates from various human and industrial sources. Pharmaceutical industries are major contributors, as they often release waste containing residual antibiotics during production processes. Hospitals and healthcare facilities also play a significant role, disposing of effluents containing unused or metabolized antibiotics directly into wastewater systems. Agricultural practices further exacerbate the issue: TCH is commonly used in animal husbandry for disease prevention and growth promotion, and antibiotics from livestock waste often enter nearby water bodies through runoff during irrigation or rainfall. Additionally, improper disposal of expired antibiotics by individuals adds to the contamination, as these medications end up in sewage systems or landfill leachates, eventually infiltrating aquatic ecosystems.[6] [7] [8]

1.6. Several techniques used for the decontamination of water

There are several techniques employed for the decontamination of water from Tetracycline Hydrochloride (TCH), each with its own advantages and mechanisms. Here are some commonly used methods:

1. **Advanced Oxidation Processes (AOPs):** These involve the generation of highly reactive radicals, such as hydroxyl radicals, through methods like UV irradiation

combined with hydrogen peroxide or persulfate. These radicals effectively break down TCH into less harmful compounds.

2. Adsorption: Materials like activated carbon, hydrochar, and modified adsorbents are used to adsorb TCH from water. This method is cost-effective and widely studied for its efficiency in removing antibiotics.

3. Membrane Filtration: Techniques such as reverse osmosis and nanofiltration are employed to physically separate TCH molecules from water. These methods are highly effective but can be expensive.

4. Biodegradation: Certain microorganisms are capable of breaking down TCH in water. This method is sustainable but may require optimization for large-scale applications.

5. Electrochemical Methods: Electrochemical oxidation processes use electrodes to degrade TCH in water. These methods are efficient but require advanced setups.

6. Photocatalysis: It is a highly efficient and sustainable method for the decontamination of water, offering significant advantages over conventional techniques in addressing pollutants like Tetracycline Hydrochloride (TCH). Unlike adsorption and membrane filtration, which only transfer contaminants to another medium, photocatalysis achieves complete mineralization, breaking down TCH into environmentally benign substances such as water and carbon dioxide. This **eco-friendly** approach utilizes light energy, thereby reducing dependence on non-renewable resources and avoiding the generation of secondary waste. Additionally, photocatalysts can often be reused multiple times without significant loss of efficiency, making the process **cost-effective** and **sustainable**. Furthermore, photocatalysis demonstrates remarkable versatility in degrading a wide array of persistent pollutants, including antibiotics resistant to conventional treatment methods. Its scalability for large-scale water treatment applications also underscores its potential as a practical and adaptable solution to the growing issue of water contamination. By leveraging light-driven processes, photocatalysis emerges as a promising and environmentally sound strategy for mitigating the challenges posed by TCH pollution.[9] [10]

1.7. Literature Review

In recent years, environmental contamination caused by pharmaceutical residues has emerged as a critical global concern. Among these, tetracycline hydrochloride (TCH)—a widely used antibiotic—has been frequently detected in aquatic ecosystems, raising alarms over its persistence and ecological impact. The presence of TCH in water bodies, even at nanogram per litre (ng/L) concentrations, contributes to antibiotic resistance, bioaccumulation, and adverse effects on aquatic organisms, disrupting microbial communities and threatening biodiversity. Given its extensive use in human medicine and animal husbandry, improper disposal and wastewater effluents further exacerbate its accumulation in the environment. Addressing TCH degradation is essential to mitigate these risks, safeguard water quality, and develop efficient treatment methods, such as advanced oxidation processes and bioremediation strategies, to eliminate pharmaceutical pollutants. [11] [12] [13]

Some photocatalytic materials, especially semiconductors, are widely studied because they have useful optical properties and adjustable electronic structures. One such material is graphitic carbon nitride (g-C_3N_4), a semiconductor that does not contain metal elements in its composition that is gaining attention for its ideal band gap (~2.7 eV), strong chemical stability, and easy production using inexpensive substances like urea. However, it has some drawbacks, such as inefficient charge separation, quick recombination of excited electrons and holes, and a limited ability to absorb visible light, which reduces its overall efficiency. To improve its performance, researchers have tried different methods, including adding elements, modifying its structure, and combining it with other semiconductors to enhance its photocatalytic abilities.[4] [5]

Fluorine doping in graphitic carbon nitride (g-C_3N_4) is a promising strategy for enhancing its photocatalytic efficiency by modifying its electronic and structural properties. The interaction of fluorine atoms with bay carbon sites alters the hybridization from sp^2 to sp^3, disrupting the conjugated system and leading to an increase in band gap energy, which directly affects charge transfer and redox potential. This modification enhances visible light absorption and process of isolating charges generated by photons to enhance efficiency in various applications, minimizing recombination losses. Additionally, fluorine doping promotes exfoliation, resulting in a modified layered structure with increased surface area that improves the accessibility of reactive sites for catalytic reactions. These

combined effects make fluorinated g-C_3N_4 (F-g-C_3N_4) highly effective for applications such as pollutant degradation. [39]

Zinc Indium Sulfide ($ZnIn_2S_4$) is a highly suitable material for constructing a heterostructure with fluorinated graphitic carbon nitride (F-g-C_3N_4) due to its advantageous electronic characteristics, strong stability, and ability to facilitate efficient charge separation. Its layered structure increases surface area, creating numerous active sites that enhance its photocatalytic performance. One of the key advantages of $ZnIn_2S_4$ is its narrow band gap, which allows for strong visible-light absorption, making it highly effective for photocatalytic applications. Additionally, $ZnIn_2S_4$ exhibits excellent charge carrier mobility, reducing recombination losses and improving overall photocatalytic efficiency. When combined with F-g-C_3N_4, the heterostructure benefits from enhanced charge transfer, leading to improved photogenerated electron-hole separation and higher catalytic activity. [41] [42]

We report the synthesis of $ZnIn_2S_4$/F-g-C_3N_4 composites with different $ZnIn_2S_4$ concentrations (10%, 20%, 30%, and 40%) using a solvothermal method. The effectiveness of these composites in photocatalysis was evaluated by degrading tetracycline hydrochloride (TCH), a widely used antibiotic, under visible light exposure to gauge their overall performance.

CHAPTER II

Experimental Section

2.1. Chemicals used:

Melamine, Ammonium fluoride (NH_4F), Zinc Chloride ($ZnCl_2$), Indium Chloride ($InCl_3.4H_2O$), Thioacetamide (TAA), Ethanol and Distilled water.

2.2. Synthesis:

2.2.1. Synthesis of graphitic carbon nitride (g-C_3N_4)

We have synthesized bulk graphitic carbon nitride (g-C_3N_4) using thermal polycondensation. In this process, we placed 3.5 grams of melamine in a covered silica crucible and subjected it to calcination at 550°C for 3 hours in a muffle furnace, with a ramp rate of 4°C per minute. After allowing the material to cool naturally to room temperature, we uniformly ground the resulting yellow powder and stored it for further use. [24]

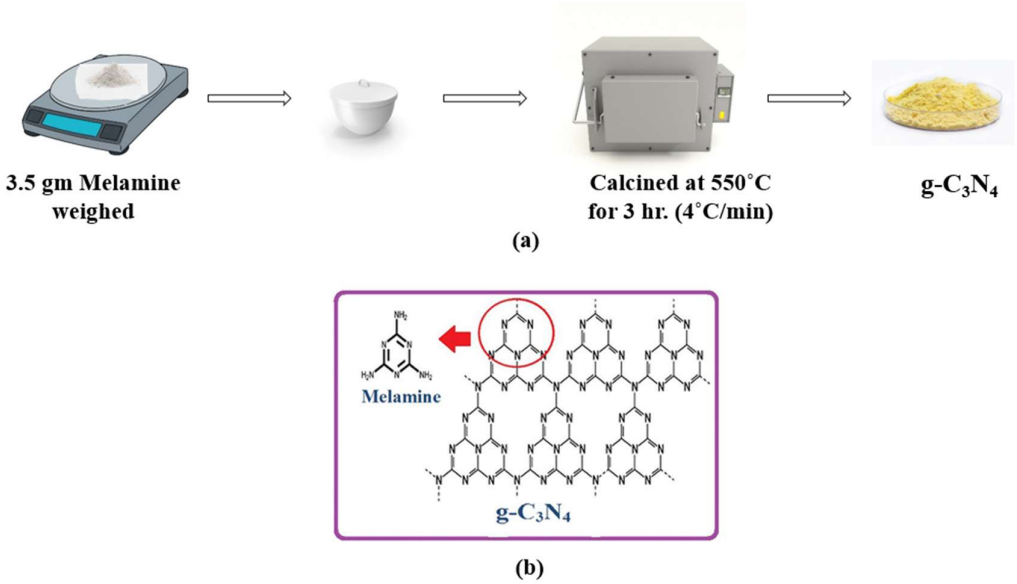

Fig. 1 (a & b) Synthesis and Structure of g-C_3N_4 (g-CN).

2.2.2. Synthesis of fluorinated-graphitic carbon nitride (F-g-C_3N_4)

We prepared fluorinated graphitic carbon nitride (F-g-C_3N_4) using a hydrothermal fluorination process. First, 1 gram of bulk g-C_3N_4 was evenly distributed in 50 mL of distilled water and subjected to ultrasonic treatment for 15 minutes to ensure an even distribution. Then, 3.5 grams of ammonium fluoride (NH_4F) was introduced into the suspension and subjected to magnetic stirring for 20 minutes to ensure uniform mixing.

Subsequently, the mixture was placed into a Teflon-lined stainless-steel autoclave, securely sealed, and heated at 180°C for 10 hours. Once cooled naturally to room temperature, the product was retrieved via centrifugation, meticulously rinsed with distilled water and ethanol until achieving a neutral pH, and subsequently dried in a vacuum oven at 70°C for 10 hours. [25] [26] [27]

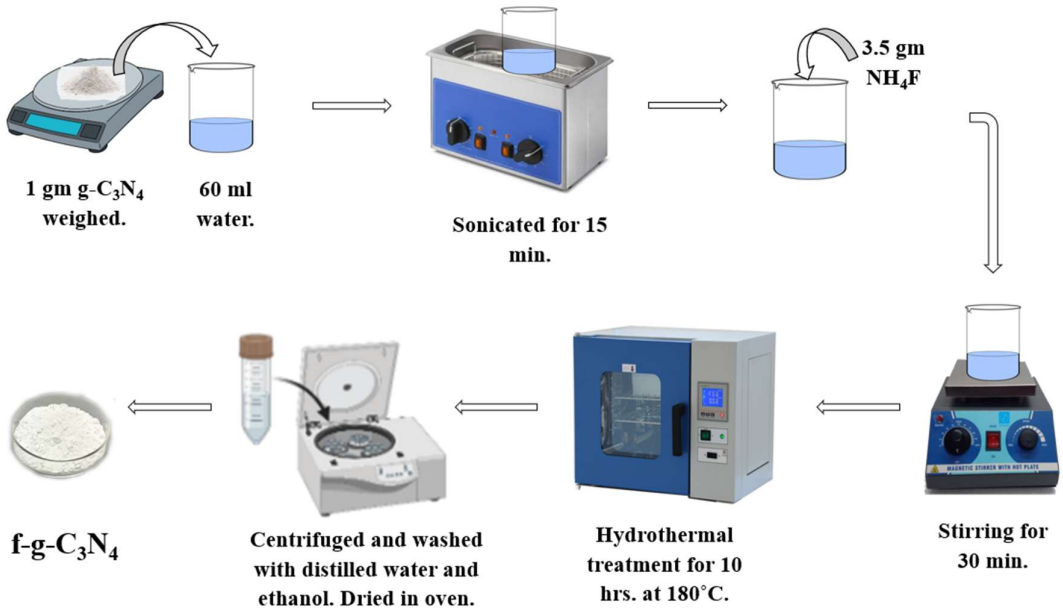
1 gm g-C_3N_4 weighed.
60 ml water.
Sonicated for 15 min.
3.5 gm NH_4F
Stirring for 30 min.
Hydrothermal treatment for 10 hrs. at 180°C.
Centrifuged and washed with distilled water and ethanol. Dried in oven.
f-g-C_3N_4

Fig. 2 Synthesis of F-g-C_3N_4 (F-gCN).

2.2.3. Synthesis of Zinc Indium Sulfide ($ZnIn_2S_4$)

We initiated the synthesis of $ZnIn_2S_4$ through a controlled solvothermal method in a water-based medium. First, we took 50 mL of distilled water and 10 mL of ethanol in a beaker, then added 1 mM of $ZnCl_2$, 4 mM of Thioacetamide (TAA), and 2 mM of $InCl_3$. The mixture underwent magnetic stirring for 30 minutes to achieve complete homogenization. Following this step, the mixture underwent solvothermal processing in an autoclave at 160°C for 12 hours. After cooling to room temperature, the product was isolated through centrifugation and purified by washing with deionized water and ethanol. Finally, we dried the material at 70°C for 12 hours, obtaining a yellow-coloured precipitate of $ZnIn_2S_4$. [39]

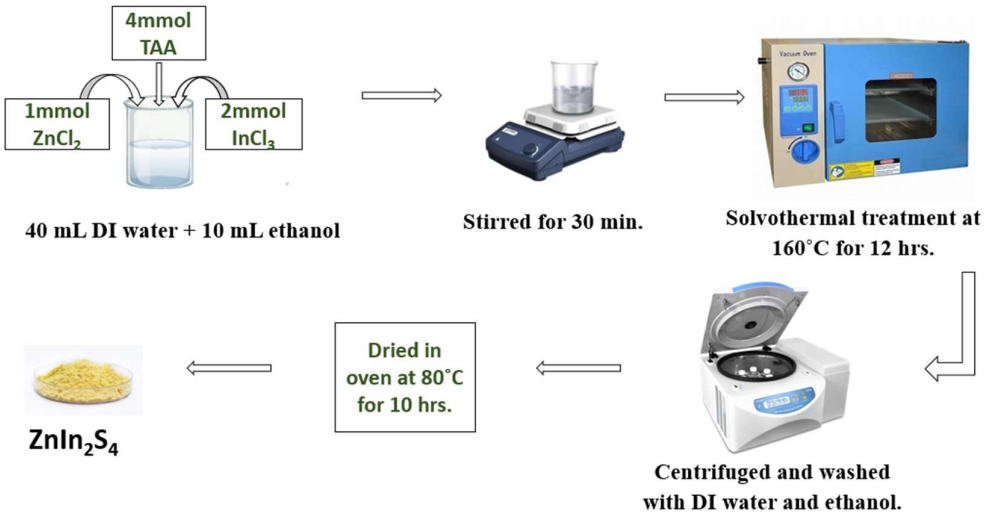

Fig. 3 Synthesis of $ZnIn_2S_4$ (ZIS).

2.2.4. Synthesis of $ZnIn_2S_4$/F-g-C_3N_4 (ZIS/F-gCN) Composites

We have synthesized $ZnIn_2S_4$/F-g-C_3N_4 composites using a one-pot solvothermal method, varying the $ZnIn_2S_4$ loading as 10, 20, 30, and 40 wt%. For the 10 wt% composite, we first ultrasonically dispersed 100 mg of F-g-C_3N_4 in a 60 mL solvent mixture of 40 mL distilled water and 20 mL ethanol. Then, we added precise amounts of $ZnCl_2$ (3.22 mg), $InCl_3 \cdot 4H_2O$ (13.85 mg), and thioacetamide (TAA, 7.1 mg) and stirred the solution magnetically for 30 minutes to ensure uniform mixing. The prepared suspension was placed in a Teflon-lined autoclave, securely sealed, and kept at 160°C for 12 hours. Once the autoclave was allowed to gradually cool down to room temperature, we collected the pale-yellow composite by centrifugation, thoroughly washed it with ethanol and distilled water, and dried it at 70°C for 10 hours. Composites with $ZnIn_2S_4$ loadings of 20, 30, and 40 wt% were synthesized using the same protocol, adjusting the precursor amounts while keeping the mass of F-g-C_3N_4 constant.

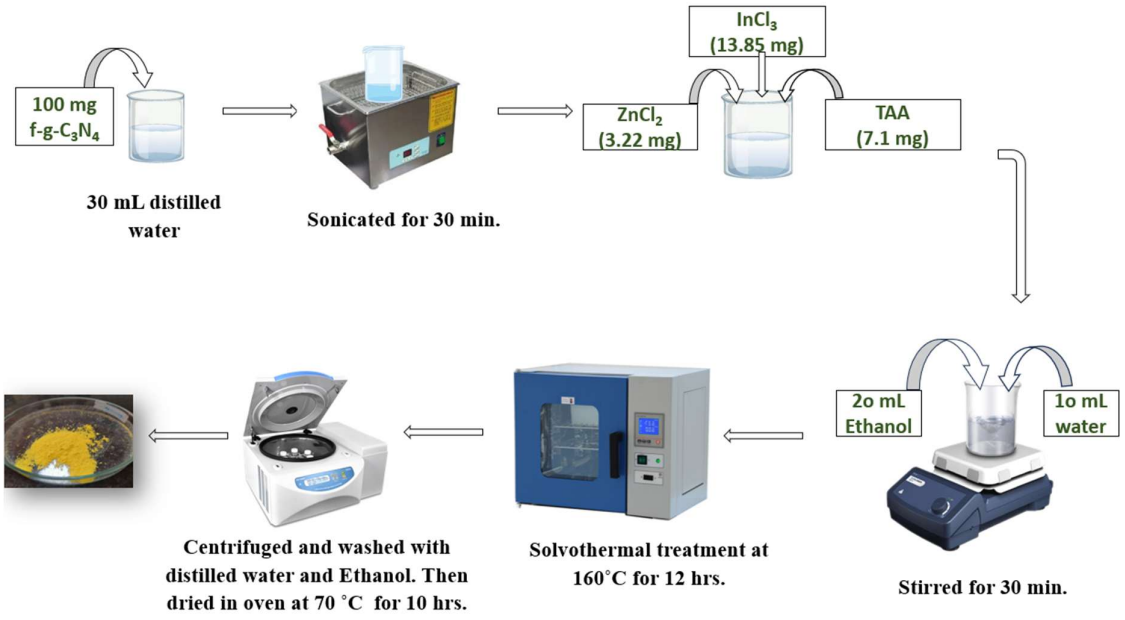
100 mg
f-g-C3N4
30 mL distilled water
Sonicated for 30 min.
InCl3 (13.85 mg)
ZnCl2 (3.22 mg)
TAA (7.1 mg)
2o mL Ethanol
1o mL water
Stirred for 30 min.
Solvothermal treatment at 160˚C for 12 hrs.
Centrifuged and washed with distilled water and Ethanol. Then dried in oven at 70 ˚C for 10 hrs.

Fig. 4 Synthesis of 10% $ZnIn_2S_4$/F-g-C_3N_4 (ZIS/F-gCN).

2.3. Characterization:

We analysed the crystalline structure and phase purity of the synthesized photocatalysts using Powder X-ray Diffraction (PXRD) on a Bruker D8 Advance ECO diffractometer with Cu Kα radiation (λ = 1.54056 Å). The optical properties, such as light absorption and band gap energy, were examined through UV-Vis Diffuse Reflectance Spectroscopy (DRS) using a Shimadzu UV-2600 spectrophotometer across a spectral range of 200–800 nm.

Thermal stability was assessed using Thermogravimetric-Differential Thermal Analysis (TG-DTA) with a Shimadzu DT-60 instrument in a nitrogen atmosphere (100 mL/min) at a heating rate of 20°C/min, covering a temperature range from 30°C to 900°C. Surface morphology and elemental distribution were characterized using Field Emission Scanning Electron Microscopy (FE-SEM) and Energy Dispersive X-Ray Spectroscopy (EDS) on a JEOL JSM-4610F instrument. [38] [25]

Detailed insights into the lattice structure and interfacial characteristics were obtained through High-Resolution Transmission Electron Microscopy (HR-TEM) conducted on an FEI Tecnai G2 F30 (300 kV) microscope. The surface chemical composition and oxidation states of the elements were examined to determine their chemical characteristics and

potential interactions through X-Ray Photoelectron Spectroscopy (XPS), using a PHI 5000 Versa Probe III system.

Finally, textural properties, including specific surface area, pore volume, and pore size distribution were assessed using nitrogen adsorption-desorption isotherms to analyse the material's porous characteristics using a Micromeritics ASAP 2020 V3.04H analyser, based on the Brunauer-Emmett-Teller (BET) method. [29]

2.4. Photocatalytic Activity Evaluation:

The $ZnIn_2S_4$/F-g-C_3N_4 composite photocatalytic efficiency was assessed through the degradation of tetracycline hydrochloride (TCH) under visible light exposure. During the experiment, 50 mg of the photocatalyst was uniformly dispersed in 100 mL of an aqueous TCH solution (20 mg/L). Prior to light irradiation, the suspension was magnetically stirred in the dark for 30 minutes to establish adsorption-desorption equilibrium.

The photocatalytic reaction was conducted under visible light illumination using five symmetrically positioned 100-W tungsten filament lamps to ensure uniform light distribution. At 10-minute intervals, 3 mL samples were extracted from the reaction mixture, centrifuged, and passed through 0.22 μm syringe filters to remove any remaining catalyst particles. The amount of tetracycline hydrochloride (TCH) present in the solution in the filtered solution was determined by measuring its absorbance at 357 nm using a UV-Visible spectrophotometer.[23]

CHAPTER III
Results and Discussion

3.1. Powder X-Ray Diffraction (PXRD):

The PXRD patterns for g-C_3N_4 (gCN), F-g-C_3N_4 (F-gCN), $ZnIn_2S_4$ (ZIS), and $ZnIn_2S_4$/F-g-C_3N_4 (ZIS/F-gCN) nanocomposites at different weight percentages are shown in Fig 9. Pristine g-C_3N_4 displays a distinct diffraction peak at 27.4º, associated with the (003) plane, this peak arises due to the interlayer stacking of conjugated aromatic systems, aligning with prior research conclusions. Following fluorination, the F-g-C_3N_4 sample retains the (003) peak, but with a noticeable increase in intensity, indicating enhanced crystallinity and potential structural modifications while preserving the g-C_3N_4 framework. The pure $ZnIn_2S_4$ sample exhibits distinct and sharp peaks at 21.7º, 27.5º, 30.5º, and 47.2º, corresponding to the (003), (011), (014), and (110) planes of its hexagonal phase, confirming its high crystallinity and phase purity.

The XRD patterns of $ZnIn_2S_4$/F-g-C_3N_4 (ZIS/FCN) composites display distinct peaks associated with both F-g-C_3N_4 and $ZnIn_2S_4$. As the $ZnIn_2S_4$ content increases from 10% to 40%, the diffraction peaks corresponding to $ZnIn_2S_4$ become more prominent and well-defined, indicating a greater crystallite presence within the composite structure. Importantly, no impurity peaks are detected, signifying that secondary phases are absent. A slight shift in the (011), (014), and (110) peaks of $ZnIn_2S_4$ within the ZIS/FCN composites suggests a successful heterojunction formation between $ZnIn_2S_4$ and F-g-C_3N_4. These findings confirm the effective integration of $ZnIn_2S_4$/F-g-C_3N_4 heterojunctions, maintaining their crystalline integrity and strong phase compatibility, making them highly suitable for enhanced charge separation and photocatalytic performance. [24] [26] [38]

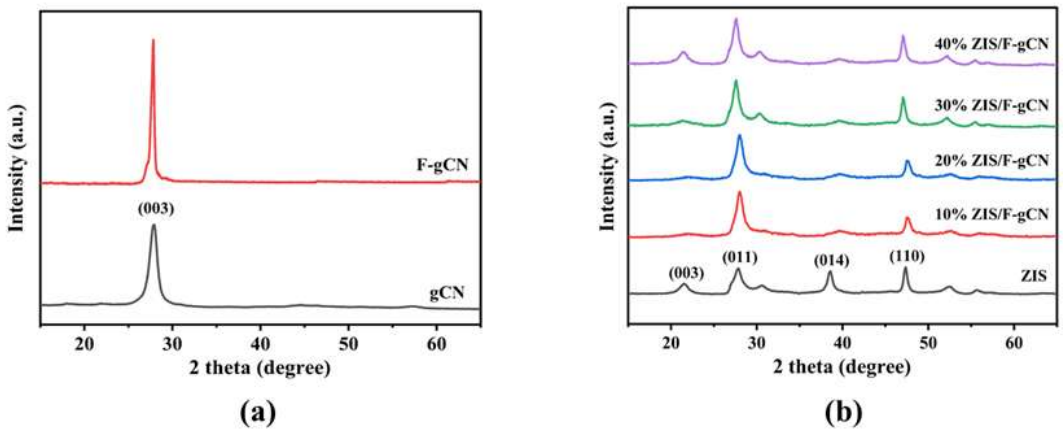

Fig. 1 (a & b) PXRD pattern of gCN, F-gCN, ZIS, and ZIS/F-gCN composites.

3.2. Field Emission Scanning Electron Microscopy (FE-SEM):

FESEM analysis of g-C_3N_4 (gCN), fluorinated g-C_3N_4 (F-gCN), and the 30% $ZnIn_2S_4$/F-g-C_3N_4 (ZIS/F-gCN) composite, presented in Figure 10, reveals their distinct surface morphologies. Pristine gCN (Figure 10 (a) and (b)) exhibits a wrinkled nanosheet structure with stacked and folded layers, characteristic of its two-dimensional nature. The sheet-like formations, offer a high surface area and porosity favourable for photocatalytic applications. Fluorination of F-gCN (Figure 10 (c) and (d)) preserved its sheet-like morphology while introducing greater roughness, partial exfoliation, and visible porosity due to structural distortions and defects caused by fluorine atoms. These changes enhance surface area and promote efficient charge separation, boosting its photocatalytic activity.

In the ZIS/F-gCN composite (Figure 10 (e) and (f)), F-gCN nanosheets act as a substrate for the uniform deposition of petal-like ZIS nanostructures. The ZIS domains, appearing as thin flakes distributed across and between F-gCN layers, ensure close interfacial contact. This well-structured heterojunction facilitates efficient division and movement of charge carriers, while the porous, hierarchical morphology enhances light absorption and reactant accessibility. FESEM analysis confirms the successful fabrication of a structurally compatible ZIS/F-gCN composite optimized for photocatalytic performance. Additionally, EDS analysis (Figure 11 (g) and elemental mapping (Figure 11 (h)) verify the presence and uniform distribution of F, C, N, Zn, In, and S, further supporting the formation of a stable heterojunction. [24] [26] [38]

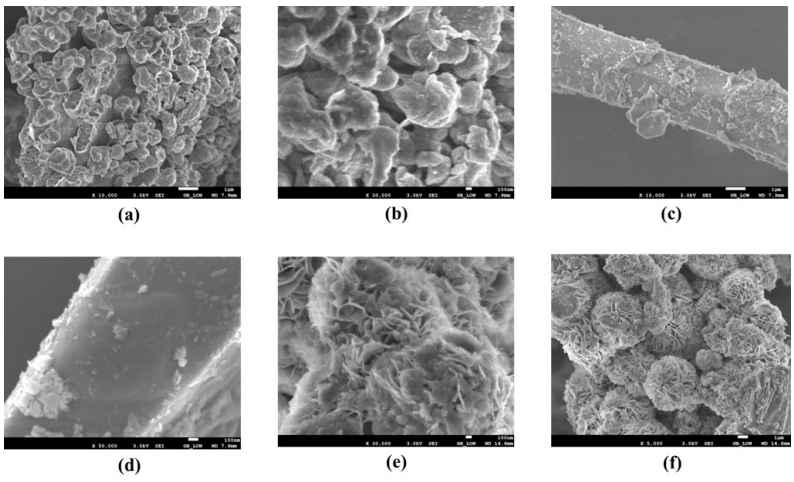

Fig. 2 FESEM images of gCN **(a-b)**, F-gCN **(c-d)**, ZIS/F-gCN **(e-f)**

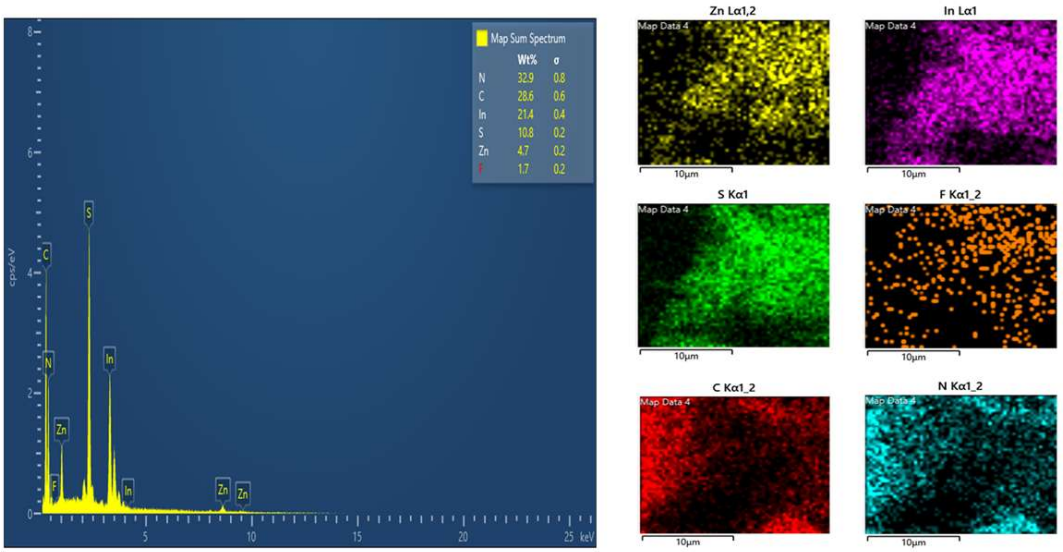

Fig. 3 (g) EDS analysis and **(h)** Elemental mapping

3.3. UV-Vis Diffuse Reflectance Spectroscopy (UV-DRS):

The optical absorption properties of gCN, F-gCN, and ZIS/F-gCN composites with varying ZIS loadings (10-40 wt%) were determined using UV-Vis Diffuse Reflectance Spectroscopy (UV-DRS) (Figure 12). All samples exhibited strong visible-light absorption, confirming their suitability for photocatalytic applications (Figure 12). Pristine gCN showed an absorption edge corresponding to a band gap of 2.71 eV, while fluorination induced a slight blue shift, increasing the band gap to 2.93 eV. This shift is attributed to fluorine's high electronegativity, which alters the electronic structure and improves charge carrier mobility by reducing defect states (Figure 13).

The addition of ZIS to the F-gCN matrix led to a red shift in the optical band edge, improving the material's ability to absorb visible light. As ZIS content increased, the band gap progressively decreased, measuring 2.90, 2.83, 2.80, and 2.50 eV for 10%, 20%, 30%, and 40% loadings, respectively (Figure 13). The most significant band gap reduction at 40% loading indicates strong electronic coupling and interfacial interaction between ZIS and F-gCN, which improves light harvesting and boosts photoinduced charge separation efficiency.[24] [27] [37]

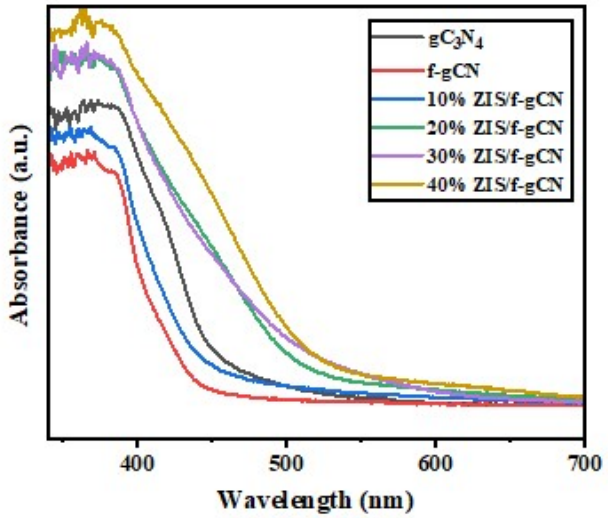

Fig. 4 UV-Vis DRS Spectrum

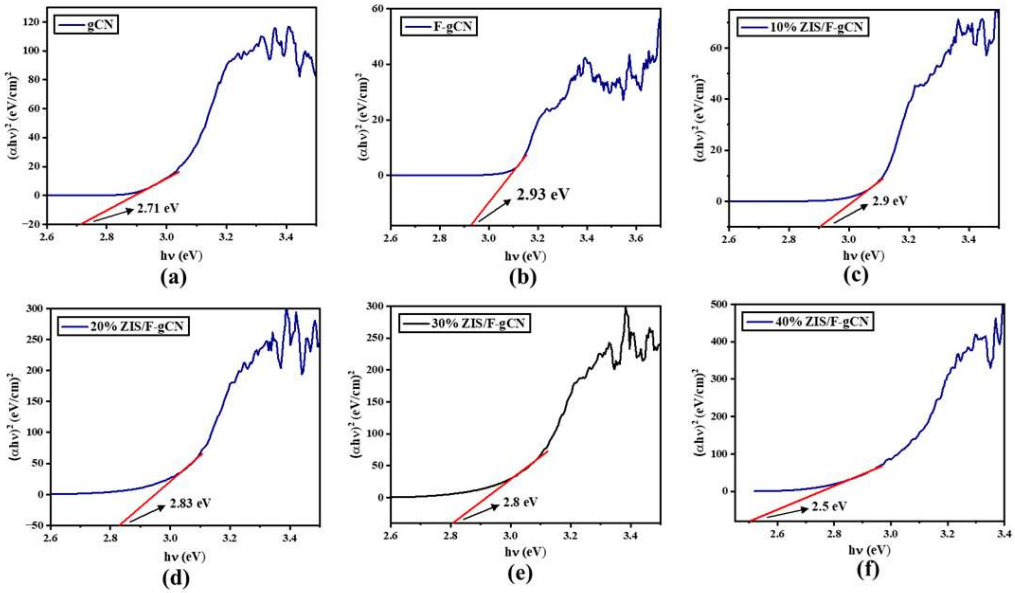

Fig. 5 Kubelka-Munk plots of gCN, F-gCN, ZIS/F-gCN with varying ZIS loadings.

3.4. X-Ray Photoelectron Spectroscopy (XPS)

To achieve a more comprehensive understanding of the chemical composition and surface characteristics, electronic properties of the 30% ZIS-F-gCN composite, high-resolution X-ray Photoelectron Spectroscopy (XPS) analysis was performed (Figure 4). The survey spectrum (Figure 3(a)) verifies the existence of Zn, In, S, F, C, and N, validating the successful formation of the composite.

As illustrated in Figure 3(b), the Zn 2p spectrum presents two distinct peaks at 1022 eV and 1045 eV, corresponding to Zn $2p_{3/2}$ and Zn $2p_{1/2}$, which are characteristic of Zn^{2+}. The In 3d region showcases two significant peaks at 444.8 eV (In 3d5/2) and 452.3 eV (In 3d3/2), signifying the presence of In^{3+} ions.

For sulfur, the S $2p_{3/2}$ and S $2p_{1/2}$ peaks, located at 161.56 eV and 162.83 eV respectively, indicate an oxidation state of -2. The F 1s spectrum, featuring a peak at 683.56 eV, confirms the successful incorporation of fluorine into the composite structure.

The C 1s spectrum reveals deconvoluted peaks at 284.7 eV (C-C), 285.9 eV (C-N), and 288.4 eV (N-C=N), characteristic of the gCN framework. The N 1s analysis identifies three distinct peaks at 398.74 eV, 399.4 eV, and 400.3 eV, linked to nitrogen in a pyridinic configuration (C=N-C), tertiary nitrogen ($N-(C)_3$), and amino groups (C-N-H), respectively.

This comprehensive analysis underscores the successful integration of various elements and structural components within the composite material.

A noticeable positive shift in the N 1s binding energies, accompanied by a negative shift in the S 2p peaks, was observed relative to the pure components, highlighting electronic interactions at the interface. These spectral changes indicate a strong interfacial coupling between ZIS and F-gCN, likely driven by N-S bonding. This interaction promotes efficient charge transfer across the heterojunction, ultimately leading to enhanced photocatalytic performance.

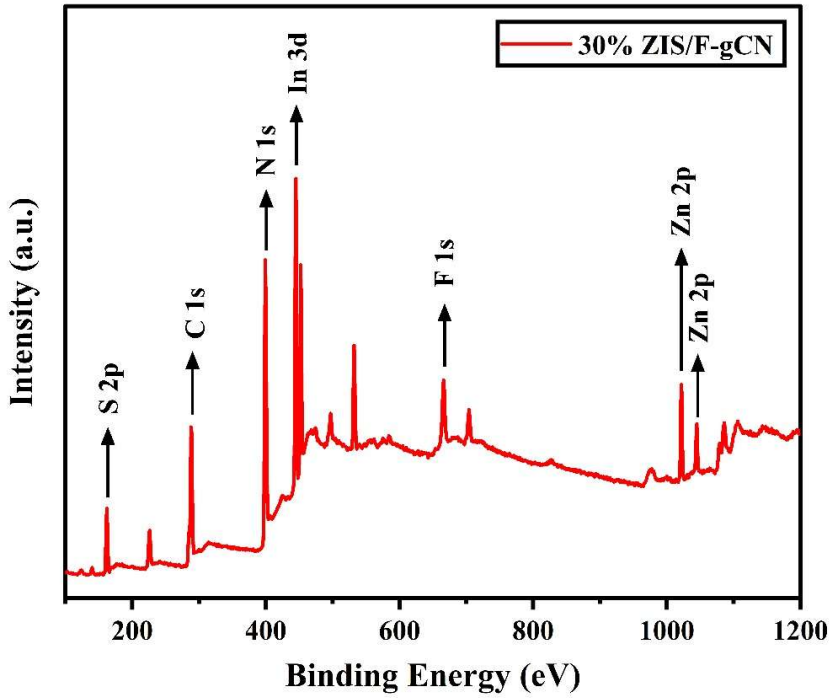

Fig. 6 Full scan and high-resolution XPS survey spectra of 30% ZIS/F-gCN.

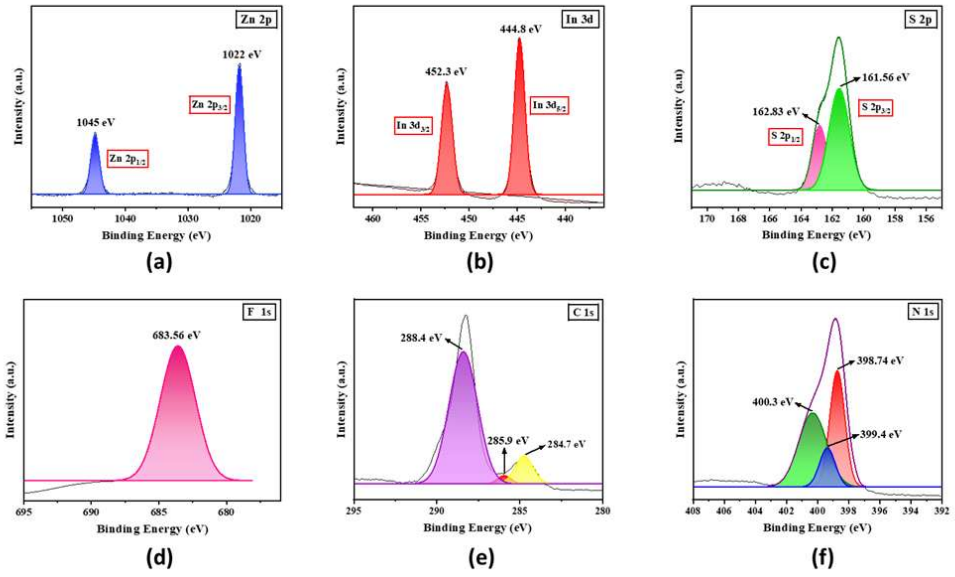

Fig. 7 Full scan and high-resolution XPS spectra of (i) Zn 2p (ii) In 3d (iii) S 2p (iv) F 1s (v) C 1s (vi) N 1s.

3.5. High-Resolution Transmission Microscopy (HR-TEM)

The microstructural properties of the 30% ZIS/F-gCN nanocomposite were examined using high-resolution transmission electron microscopy (HR-TEM), with the corresponding selected area electron diffraction (SAED) pattern displayed in Figure 5. The HR-TEM image reveals well-defined lattice fringes, showing distance between adjacent planes in a crystalline structure of approximately 0.30 nm, which corresponds to the (110) plane of hexagonal ZIS. The presence of clear and continuous fringes highlights the high crystallinity of ZIS domains embedded within the F-gCN matrix.

Additionally, the SAED pattern presents a series of bright diffraction rings, reinforcing the polycrystalline nature of the composite. These findings confirm the effective integration of ZIS nanosheets onto the F-gCN structure, ensuring the preservation of crystallinity in individual components while enhancing interfacial contact. This strong interfacial interaction is essential for optimizing charge separation and transfer, which is vital for enhancing the effectiveness of photocatalysis.

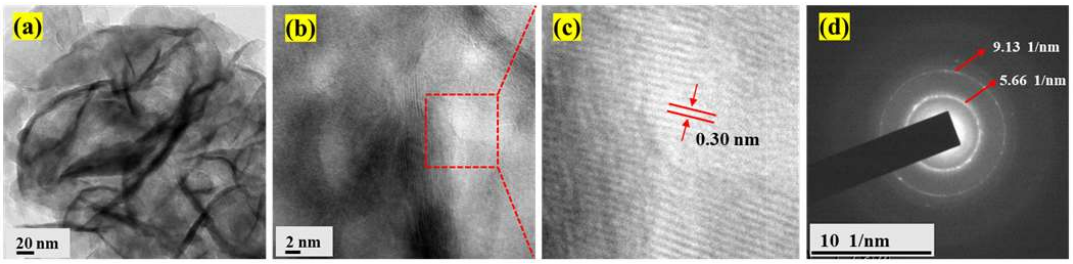

Fig. 8 HR-TEM images of 30% ZIS/F-gCN.

3.6. Thermogravimetric Analysis (TGA)

Thermogravimetric analysis (TGA) was conducted to examine the thermal decomposition behaviour of the 30% ZIS/F-gCN composite under a nitrogen atmosphere. The TGA profile reveals three distinct weight-loss stages.

The first stage, with a weight reduction of approximately 2.3% between 30 ºC and 310 ºC, is attributed to the evaporation of physically adsorbed moisture and residual organic solvents trapped within the porous structure—an effect commonly observed in gCN-based materials.

The second and most significant weight loss, around 40%, occurs between 310 ºC and 393 ºC, corresponding to the thermal breakdown of the gCN framework. This phase primarily involves the decomposition of heptazine-based units and fluorinated functional groups introduced during fluorination. Additionally, within this temperature range, partial degradation of ZIS nanosheets may take place, as metal sulfides like ZIS are susceptible to oxidation or breakdown when inert or oxidative conditions at higher temperatures.

The third stage, with an additional 14% weight loss between 393 ºC and 750 ºC, is attributed to the further decomposition of carbonaceous residues, potential structural collapse of remaining gCN fragments, and transformation of ZIS into thermally stable sulfide or oxide residues.

Overall, the composite exhibits moderate thermal stability up to 310 ºC, making it well-suited for photocatalytic applications conducted at ambient or moderately elevated temperatures.

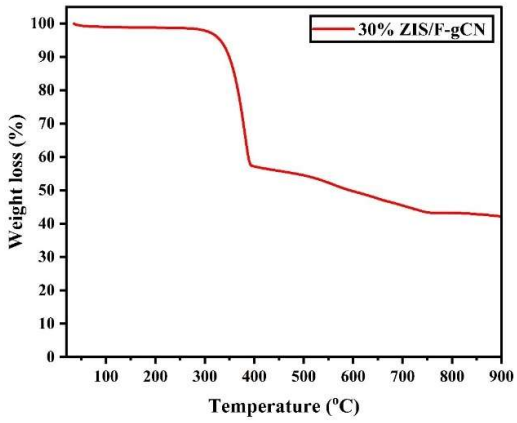

Fig. 9 Thermogravimetric Analysis of 30% ZIS/F-gCN.

3.7. Brunauer-Emmett-Teller Analysis (BET)

The nitrogen adsorption-desorption isotherm of the 30% ZIS/F-gCN composite displayed a characteristic Type IV profile, accompanied by an H3-type hysteresis loop, indicative of a mesoporous framework. A progressive increase in nitrogen uptake at intermediate relative pressures ($P/P_0 \approx 0.4–0.9$), followed by the appearance of a hysteresis loop, suggests capillary condensation occurring within mesopores. The sharp rise in adsorbed

volume at elevated relative pressures confirms the presence of larger mesopores or interparticle voids. The specific surface area, determined via the Brunauer-Emmett-Teller (BET) method, was calculated to be 52.347 m^2/g. Additionally, the Barrett-Joyner-Halenda (BJH) pore size distribution analysis highlighted dominant pore radii within the mesoporous range (2–50 nm), along with pore volume and pore radius of 0.13 cm^3/gm and 1.636 nm respectively, further validating the composite's hierarchical porous architecture, which is advantageous for photocatalytic applications.

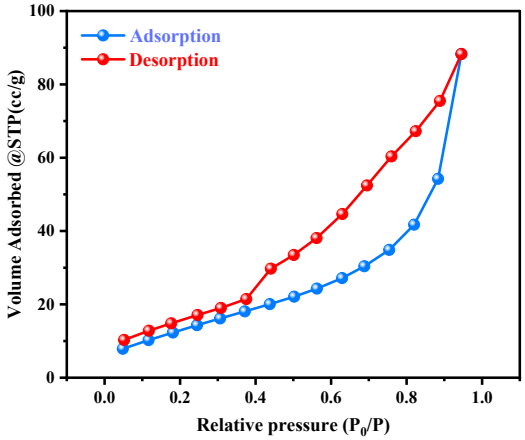

Fig. 10 N_2 adsorption-desorption isotherm for 30% ZIS/F-gCN.

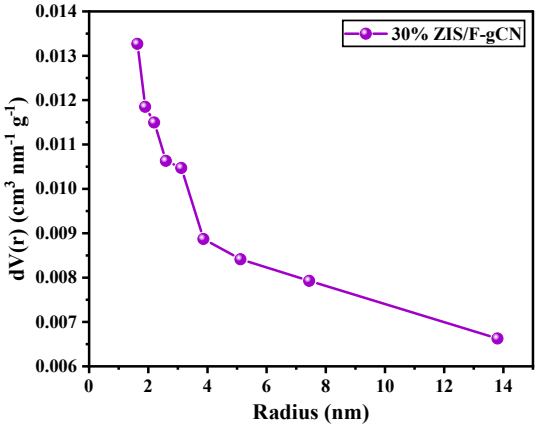

Fig. 11 Pore size distribution of 30% ZIS/F-gCN.

CHAPTER IV
Photocatalytic Experiments

4.1. Photocatalytic degradation of TCH

Photocatalytic degradation experiments were conducted using a 100 mL aqueous solution of tetracycline hydrochloride (TCH) with a concentration of 20 mg L^{-1}, with 50 mg of photocatalyst under visible light irradiation. Among the tested materials, the 30% $ZnIn_2S_4$-loaded fluorinated g-C_3N_4 (ZIS/F-gCN) composite demonstrated the highest degradation efficiency, achieving about 90% TCH removal in 90 minutes, with a pseudo-first-order rate constant (k) of 0.0263 min^{-1}. Before exposure to light, all samples underwent a 30-minute dark phase to establish adsorption-desorption equilibrium.

Optimization studies determined that a catalyst dosage of 50 mg and a solution pH of 6 yielded the most effective degradation results. Comparative analysis of photocatalytic performance across pristine gCN, F-gCN, and ZIS/F-gCN composites with different ZIS loadings (10%, 20%, 30%, and 40%) revealed degradation efficiencies of 16.4%, 36.4%, 41.1%, 64%, 90%, and 67%, respectively. The non-linear trend suggests that excessive ZIS loading may lead to particle aggregation or shielding effects, ultimately reducing light absorption and limiting the availability of active sites.

The impressive photocatalytic performance of the 30% ZIS/F-gCN composite is primarily a result of the cooperative interplay between $ZnIn_2S_4$ (ZIS) and fluorinated g-C_3N_4 (F-gCN). This interaction plays a vital role in enhancing the efficient separation of photogenerated electron-hole pairs, which substantially minimizes their recombination rate, enhancing overall performance. The incorporation of ZIS into the F-gCN matrix creates an optimized heterojunction structure, which facilitates efficient charge transfer and promotes prolonged charge carrier lifetimes. As a result, the composite exhibits superior photocatalytic activity when exposed to visible light. Moreover, the fluorination of g-C_3N_4 contributes to improved charge mobility and enhances light absorption properties, further boosting the overall degradation efficiency. This well-balanced combination of structural and electronic properties ensures that the composite achieves a high degree of pollutant removal while maintaining stable performance throughout the reaction process. [42] [30]

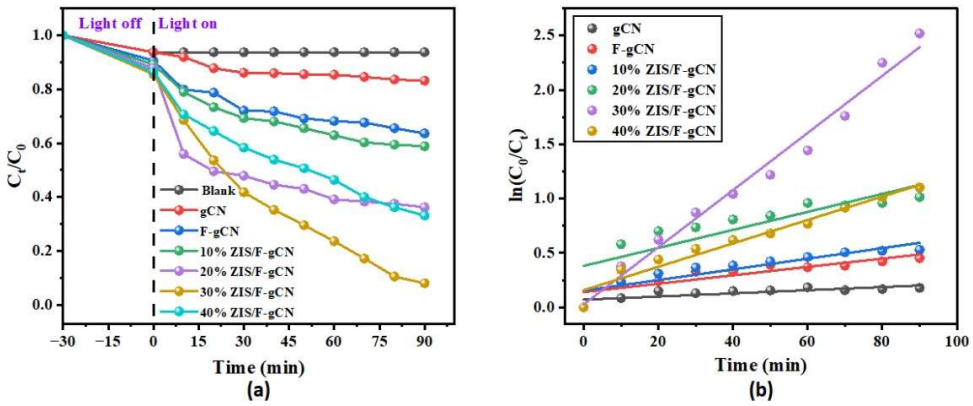

Fig. 1 (a) TCH Degradation experiments for blank (no catalyst), gCN, F-gCN, ZIS/F-gCN composites with varying ZIS loadings. **(b)** Rate constant plot for gCN, F-gCN, ZIS/F-gCN composites with varying ZIS loadings.

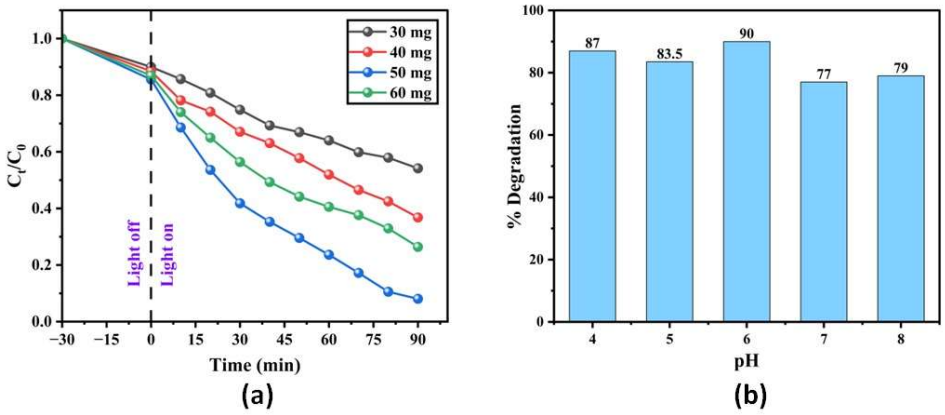

Fig. 2 (a) Effect of catalyst dose on photocatalytic TCH degradation using 30% ZIS/F-gCN composite under visible light irradiation (20 mg L^{-1}, 100 mL, pH 6) **(b)** Effect of initial pH on photocatalytic TCH degradation using 30% ZIS/F-gCN composite under visible light irradiation (20 mg L^{-1}, 100 mL, 50 mg catalyst)

4.2. Plausible Mechanism

The improved photocatalytic performance is predominantly driven by the formation of a type-II heterojunction, which enables efficient charge carrier separation. Based on experimentally determined band gaps and electronegativity values, the conduction and valence band positions of fluorinated g-C_3N_4 (F-gCN) are estimated to be -1.235 eV and +1.695 eV, respectively, while $ZnIn_2S_4$ (ZIS) exhibits conduction and valence band positions at -0.8 eV and +1.9 eV compared to the normal hydrogen electrode (NHE). Under visible light irradiation, both semiconductors become excited, generating electron-hole pairs. Electrons from the conduction band of F-gCN transfer to the conduction band of ZIS, while holes in the valence band of ZIS move toward the more positively charged valence band of F-gCN, facilitating charge separation. This process leads to enhanced spatial charge separation and minimized recombination, characteristic of an efficient type-II heterojunction system, enhancing the composite's photocatalytic efficiency.

The electrons transferred within $ZnIn_2S_4$ (ZIS) facilitate the reduction of dissolved oxygen (O_2), leading to the formation of superoxide radicals ($\bullet O_2^-$), which have been identified through quenching experiments as the primary reactive specie responsible for the degradation of tetracycline hydrochloride (TCH). Simultaneously, the holes present in fluorinated g-C_3N_4 (F-gCN) contribute to oxidation reactions, including the formation of hydroxyl radicals (•OH) via water oxidation. The relative impact of these reactive species, as determined by scavenger studies, follows the sequence: $\bullet O_2^- > h^+ > \bullet OH > e^-$. These reactive species are responsible for the degradation of Tetracycline Hydrochloride (TCH) into harmless degraded products like CO_2, H_2O. This mechanistic analysis emphasizes the pivotal role of superoxide radicals in the degradation process and highlights the beneficial synergistic interactions occurring within the ZIS/F-gCN heterojunction system.

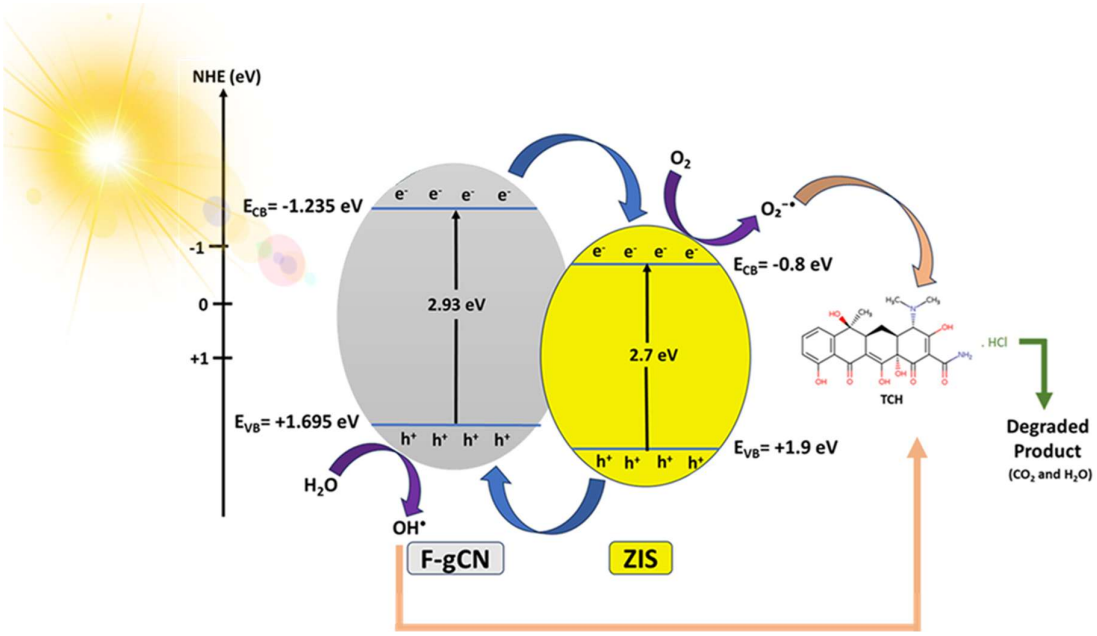

Fig. 3 Plausible Mechanism for TCH degradation.

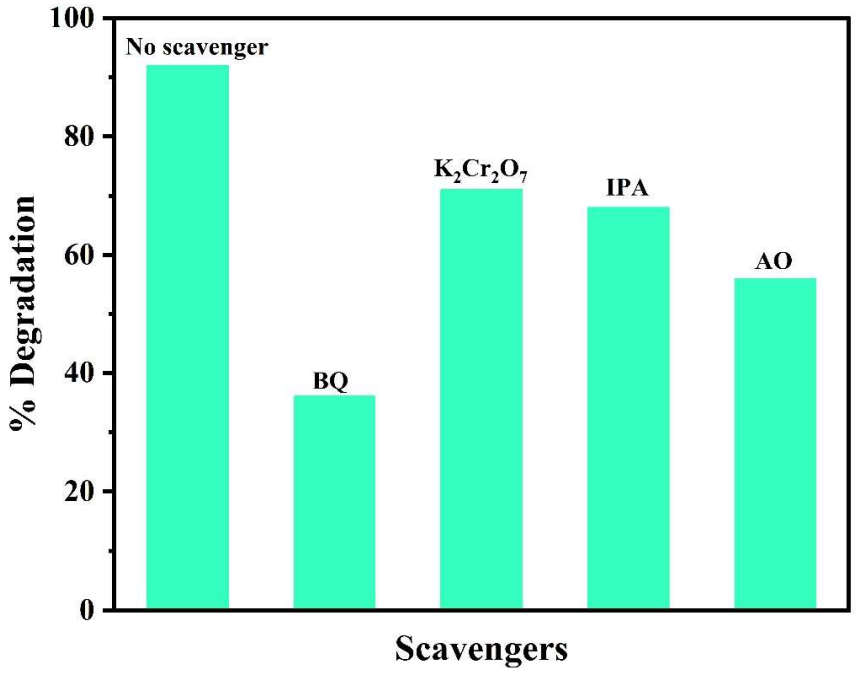

Fig. 4 Quenching Experiment for TCH degradation.

4.3. Recyclability Test of the Photocatalyst

The reusability of the optimized 30% ZIS/F-gCN photocatalyst was assessed through multiple successive photocatalytic breakdown stages of tetracycline hydrochloride (TCH) under exposure to visible light. After each cycle, the catalyst was retrieved via centrifugation, thoroughly rinsed with distilled water and ethanol, followed by drying for reuse. The composite consistently maintained high photocatalytic efficiency, exhibiting only a slight decline in performance over repeated cycles. This demonstrates its strong stability and durability, strengthening its viability for real-world applications in sustainable environmental cleanup and restoration over extended periods.

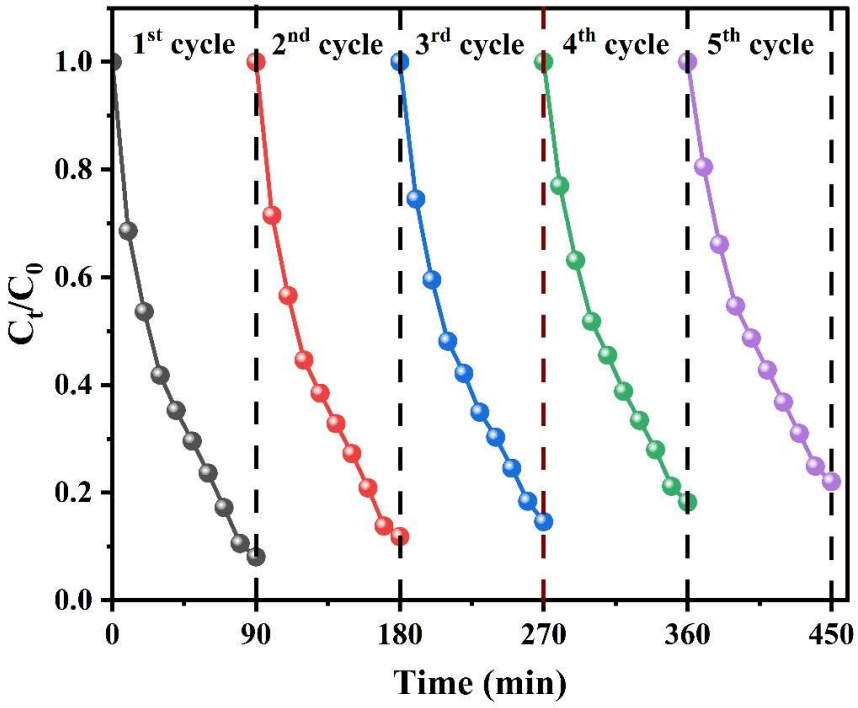

Fig. 5 The recyclability test of photocatalytic TCH degradation for 30% ZIS/F-gCN.

Conclusion

In conclusion, a series of $ZnIn_2S_4$/F-gC_3N_4 (ZIS/F-gCN) heterostructure composites were effectively fabricated through a solvothermal approach, with the 30 wt% $ZnIn_2S_4$ loading exhibiting maximum level of photocatalytic performance, achieving optimal degradation effectiveness under given conditions. The remarkable degradation rate of 90% for tetracycline hydrochloride (TC-HCl) under visible light within 90 minutes can be attributed to the combined effects of fluorination-induced electronic tuning in g-C_3N_4 and the formation of a closely connected 2D/2D heterojunction interface. This structural arrangement enabled extended light absorption and significantly enhanced charge carrier separation and mobility, as verified through detailed characterization and radical scavenging studies. Additionally, active species trapping experiments confirmed that superoxide radicals ($\bullet O_2^-$) played the dominant role in the photocatalytic degradation mechanism. The 30% ZIS/F-gCN composite also exhibited outstanding stability and reusability, retaining high photocatalytic efficiency across five successive cycles without substantial performance deterioration, reinforcing its practicality for long-term environmental remediation applications.

References:

[1] D.B. Wang, F.Y. Jia, H. Wang, F. Chen, Y. Fang, W.B. Dong, G.M. Zeng, X.M. Li, Q. Yang, X.Z. Yuan, simultaneously efficient adsorption and photocatalytic degradation of tetracycline by Fe-based MOFs, J. Colloid Interface Sci. 519 (2018) 273–284, https://doi.org/10.1016/j.jcis.2018.02.067.

[2] C. Song, B.-B. Guo, X.-F. Sun, S.-G. Wang, Y.-T. Li, Enrichment and degradation of tetracycline using three-dimensional graphene/MnO_2 composites, Chem. Eng. J 358 (2019) 1139–1146, https://doi.org/10.1016/j.cej.2018.10.119.

[3] Y. Zhang, S. Zuo, Y. Zhang, G. Ren, Y. Pan, Q. Zhang, M. Zhou, Simultaneous removal of tetracycline and disinfection by a flow-through electro-peroxone process for reclamation from municipal secondary effluent, J. Hazard. Mater 368 (2019) 771–777, https://doi.org/10.1016/j.jhazmat.2019.02.005.

[4] Y. Pan, Y. Zhang, M. Zhou, J. Cai, Y. Tian, Enhanced removal of emerging contaminants using persulfate activated by UV and pre-magnetized Fe^0, Chem. Eng. J. 361 (2019) 908–918, https://doi.org/10.1016/j.cej.2018.12.135.

[5] J. Chen, X. Zhang, F. Bi, X. Zhang, Y. Yang, Y. Wang, A facile synthesis for uniform tablet-like TiO_2 /C derived from Materials of Institute Lavoisier-125(Ti) (MIL-125 (Ti)) and their enhanced visible light-driven photodegradation of tetracycline, J. Colloid Interface Sci. 571 (2020) 275–284, https://doi.org/10.1016/j. jcis.2020.03.055.

[6] M. Yan, Y. Yan, Y. Wu, W. Shi, Y. Hua, Microwave-assisted synthesis of monoclinic- tetragonal $BiVO_4$ heterojunctions with enhanced visible-light-driven photocatalytic degradation of tetracycline, RSC Adv. 5 (110) (2015) 90255–90264.

[7] E.T. Helmy, E.M. Abouellef, U.A. Soliman, J.H. Pan, Novel green synthesis of S- doped TiO_2 nanoparticles using Malva parviflora plant extract and their photocatalytic, antimicrobial and antioxidant activities under sunlight illumination, Chemosphere 271 (2021) 129524, https://doi.org/10.1016/j. chemosphere.2020.129524.

[8] M. Guan, C. Xiao, J. Zhang, S. Fan, R. An, Q. Cheng, J. Xie, M. Zhou, B. Ye, Y.i. Xie, Vacancy associates promoting solar-driven photocatalytic activity of ultrathin bismuth oxychloride nanosheets, J. Am. Chem. Soc. 135 (28) (2013) 10411–10417, https://doi.org/10.1021/ja402956f.

[9] J. Li, X. Wu, W. Pan, G. Zhang, H. Chen, Vacancy-Rich Monolayer BiO_2 as a Highly Efficient UV, Visible, and Near-Infrared Responsive Photocatalyst, Angew. Chem. Int. Ed. 57 (2) (2018) 491–495, https://doi.org/10.1002/anie.201708709.

[10] N. Zhang, X. Li, H. Ye, S. Chen, H. Ju, D. Liu, Y. Lin, W. Ye, C. Wang, Q. Xu, J. Zhu, L.i. Song, J. Jiang, Y. Xiong, Oxide Defect Engineering Enables to Couple Solar Energy into Oxygen Activation, J. Am. Chem. Soc. 138 (28) (2016) 8928–8935, https://doi.org/10.1021/jacs.6b04629

[11] J.H. Pan, J. Schneider, W.Y. Teoh, Photocatalysis for environmental remediation - From laboratories to industry and beyond, Chemosphere 286 (2022) 131704, https://doi.org/10.1016/j.chemosphere.2021.131704.

[12] D. Cui, L. Wang, K. Xu, L. Ren, L.i. Wang, Y. Yu, Y.i. Du, W. Hao, Band-gap engineering of BiOCl with oxygen vacancies for efficient photooxidation properties under visible-light irradiation, J. Mater. Chem. A 6 (5) (2018) 2193–2199, https:// doi.org/10.1039/C7TA09897A.

[13] M. Misra, S.R. Chowdhury, T.I. Lee, Sunlight driven decomposition of toxic organic compound, coumarin, p-nitrophenol, and photo reduction of Cr(VI) ions, using a bridge structure of Au@CNT@TiO_2 nanocomposite, Appl. Catal. B-Environ. 272 (2020) 118991–119003.

[14] J. Huang, B.S. Wang, Z.J. Hao, Z.R. Zhou, Y. Qu, Boosting charge separation and broadening NIR light response over defected WO_3 quantum dots coupled g-C_3N_4 nanosheets for photocatalytic degrading antibiotics, Chem. Eng. J. 416 (2021) 129109–129123.

[15] P. Chen, Y.J. Gou, J.M. Ni, Y.M. Liang, B.Q. Yang, F.F. Jia, S.X. Song, Efficient Ofloxacin degradation with Co(II)-doped MoS_2 nano-flowers as PMS activator under visible-light irradiation, Chem. Eng. J. 401 (2020) 125978–125988.

[16] A. Verma, S. Kumar, Y.P. Fu, A ternary-hybrid as efficiently photocatalytic antibiotic degradation and electrochemical pollutant detection, Chem. Eng. J. 408 (2021) 127290–127306.

[17] S.S. Xin, G.C. Liu, X.H. Ma, J.X. Gong, B.R. Ma, Q.H. Yan, Q.H. Chen, D. Ma, G. S. Zhang, M.C. Gao, Y.J. Xin, High efficiency heterogeneous fenton-like catalyst biochar modified CuFeO2 for the degradation of tetracycline: economical synthesis, catalytic performance and mechanism, Appl. Catal. B-Environ. 280 (2021) 119386.

[18] C.H. Han, H.D. Park, S.B. Kim, V. Yargeau, J.W. Choi, S.H. Lee, J.A. Park, Oxidation of tetracycline and oxytetracycline for the photo-fenton process: their transformation products and toxicity assessment, Water Res. 172 (2020) 115514.

[19] Z. Song, Y.L. Ma, C.E. Li, M. Xu, C. Zhang, Molecular sieving film prepared by vacuum filtration for the efficient removal of tetracycline antibiotics from pharmaceutical wastewater, Adv. Mater. Sci. Eng. 2019 (2019) 3532576.

[20] M.H. Liu, J.F. Luo, P. Shukla, Effluents detoxification from pulp and paper industry using microbial engineering and advanced oxidation techniques, J. Hazard. Mater. 398 (2020) 122998.

[21] S.A.C. Carabineiro, T. Thavorn-amornsri, M.F.R. Pereira, P. Serp, J.L. Figueiredo, Comparison between activated carbon, carbon xerogel and carbon nanotubes for the adsorption of the antibiotic ciprofloxacin, Catal. Today 186 (2012) 29–34.

[22] C. Jin, K. Su, L. Tan, X.M. Liu, Z.D. Cui, X.J. Yang, Z.Y. Li, Y.Q. Liang, S.L. Zhu, K. W.K. Yeung, S.L. Wu, Near-infrared light photocatalysis and photothermy of carbon quantum dots and au nanoparticles loaded titania nanotube array, Mater. Des. 177 (2019) 107845.

[23] F. Dong, T. Xiong, Y. Sun, L. Lu, Y. Zhang, H. Zhang, H. Huang, Y. Zhou, Z. Wu, Exploring the photocatalysis mechanism on insulators, Appl. Catal. B-Environ. 219 (2017) 450–458.

[24] C.Q. Li, Z.M. Sun, W.Z. Zhang, C.H. Yu, S.L. Zheng, Highly efficient g-C3N4/TiO2/ kaolinite composite with novel three-dimensional structure and

enhanced visible light responding ability towards ciprofloxacin and S. aureus, Appl. Catal. B- Environ. 220 (2018) 272–282.

[25] L. Zhang, X. Hao, Y. Li, Z. Jin, Performance of WO3/g-C3N4 heterojunction composite boosting with NiS for photocatalytic hydrogen evolution, Appl. Surf. Sci. 499 (2020): 143862.

[26] X. Wang, K. Maeda, A. Thomas, K. Takanabe, G. Xin, J.M. Carlsson, K. Domen, M. Antonietti, Nat. Mater. 8 (2009) 76–80.

[27] W.J. Ong, L.L. Tan, Y.H. Ng, S.T. Yong, S.P. Chai, Chem. Rev. 116 (2016) 7159–7329.

[28] Z. Zhao, Y. Sun, F. Dong, Nanoscale 7 (2015) 15–37. [18] S.M. Lam, J.C. Sin, A.R. Mohamed, Mater. Sci. Semicond. Process. 47 (2016) 62–84.

[29] L.B. Jiang, X.Z. Yuan, Y. Pan, J. Liang, G.M. Zeng, Z.B. Wu, H. Wang, Appl. Catal. B: Environ. 217 (2017) 388–406.

[30] Y.J. Zhang, T. Mori, J.H. Ye, M. Antonietti, J. Am. Chem. Soc. 132 (2010) 6294.

[31] G.D. Ding, W.T. Wang, T. Jiang, B.X. Han, H.L. Fan, G.Y. Yang, ChemCatChem 5 (2013) 192–200.

[32] B. Chai, J. Yan, C. Wang, Z. Ren, Y. Zhu, Appl. Surf. Sci. 391 (2017) 376–383.

[33] N. Sagara, S. Kamimura, T. Tsubota, T. Ohno, Appl. Catal. B: Environ. 192 (2016) 193–198.

[34] Y. Li, S. Wu, L. Huang, J. Wang, H. Xu, H. Li, Mater. Lett. 137 (2014) 281–284.

[35] S. Guo, Y. Zhu, Y. Yan, Y. Min, J. Fan, Q. Xu, Appl. Catal. B: Environ. 185 (2016) 315–321.

[36] K. Wang, Q. Li, B. Liu, B. Cheng, W. Ho, J. Yu, Appl. Catal. B: Environ. 176–177 (2015) 44–52.

[37] Q. Fan, J. Liu, Y. Yu, S. Zuo, B. Li, Appl. Surf. Sci. 391 (2017) 360–368.

[38] L.B. Jiang, X.Z. Yuan, G.M. Zeng, X.H. Chen, Z.B. Wu, J. Liang, J. Zhang, H. Wang, H. Wang, ACS Sustainable Chem. Eng. 5 (2017) 5831–5841.

[39] Y. Wang, Y. Di, M. s Antonietti, H.R. Li, X.F. Chen, X.C. Wang, Chem. Mater. 22 (2010) 5119–5121. [30] F.K. Ma, C.L. Sun, Y.L. Shao, Y.Z. Wu, B.B. Huang, X.P. Hao, New J. Chem. 41 (2017) 3061–3067.

[40] Z. Guan, J. Pan, Q. Li, G. Li, and J. Yang, “Boosting Visible-Light Photocatalytic Hydrogen Evolution with an Efficient $CuInS_2$ /$ZnIn_2S_4$ 2D/2D Heterojunction,” ACS Sustain Chem Eng, vol. 7, no. 8, 2019, doi: 10.1021/acssuschemeng.8b06587.

[41] Z.L. A, M.Z. A, L.Z. A, C.D. A, J.M. A, Z.W. A, H.L. A, H.W. B, Aqueous tetracycline degradation by coal-based carbon electrocatalytic filtration membrane: effect of nano antimony-doped tin dioxide coating, Chem. Eng. J. 314 (2017) 59–68.

[42] L. Lan, X. Kong, H. Sun, C. Li, D. Liu, High removal efficiency of antibiotic resistance genes in swine wastewater via nanofiltration and reverse osmosis processes, J. Environ. Manag. 231 (2019) 439–445.

[43] W. Li, Q. Chen, X. Lei, S. Gong, Fabrication of Ag/AgBr/Ag3VO4 composites with high visible light photocatalytic performance, RSC Adv. 9 (2019) 5100–5109.

Future Scope:

This study highlights the promising performance of 30% ZIS/F-g-C_3N_4 composite for visible-light-driven degradation of tetracycline hydrochloride. To further enhance its application potential, future work can focus on:

- **Expanding pollutant scope** to include a wider range of contaminants in real wastewater matrices.
- **In-depth mechanistic studies** using advanced techniques (e.g., EPR, in situ FTIR) to clarify reactive species and degradation pathways.
- **Scaling up** through immobilization on supports for practical photocatalytic reactors.
- **Exploring dual functionality**, such as simultaneous hydrogen evolution and pollutant degradation.
- **Further modifications**, like co-doping or integrating with other 2D materials, to improve charge separation and light absorption.